J. Fluid Mech. (2005), *vol.* 540, *pp.* 143–173.
doi:10.1017/S0022112005005690 Printed in the United Kingdom

Rotational and translational dispersion of fibres in isotropic turbulent flows

By MANSOO SHIN AND DONALD L. KOCH

School of Chemical and Biomolecular Engineering, Cornell University, Ithaca, NY 14853, USA

(Received 31 July 2004 and in revised form 11 April 2005)

The rotational and translational motions of fibres in fully developed isotropic turbulence are simulated for a range of turbulence Reynolds numbers. Equations for fibre motion based on the leading-order slender-body theory relate the fibre's translational and rotational velocities to zeroth and first moments of the fluid velocity along the fibre length. The translational and rotational motions of fibres with lengths that exceed the size of the smallest eddies are attenuated by the filtering associated with these spatial averages. The translational diffusivity of the fibres can be predicted using a simple theory that neglects any coupling between fibre orientation and the local direction of the fluid velocity. However, the coupling of fibre orientation with the axes of extension and rotation is found to greatly reduce the amplitude of the rotary motions and the rotational dispersion coefficient. The rotary dispersion coefficient is found to be on the order of the inverse integral time scale. However, its variation with Reynolds number suggests that the rotary dispersion is influenced by all the scales of turbulence over the limited range of Reynolds numbers explored in our simulations.

1. Introduction

In this paper, we present results of direct numerical simulations of the translational and rotational motion of slender fibres in isotropic turbulence. A parametric study is conducted to determine how the fibres' translational and rotational dispersion depends on fibre length and the Reynolds number of the turbulent flow. Whenever possible, the numerical results will be compared with simple theories and/or scaling arguments to help clarify the mechanisms governing fibre motion.

The rotational and translational dispersion of fibres in turbulent flows plays an important role in process such as paper-making, blowing of fibre glass insulation, drag reduction, and remediation of indoor air pollution. Turbulence tends to create an isotropic fibre orientation distribution during paper-making and fibre-glass blowing. This dispersion of fibre orientation may have a desirable effect on material properties. In risk assessment and remediation of problems involving contamination of indoor air by long slender asbestos fibres, it is important to know how the fibres are dispersed by the turbulent air flow. Small concentrations of polymers or high-aspect-ratio fibres can greatly reduce the pressure drop or drag in a turbulent flow (Daily & Bugliarello 1961; Mih & Parker 1967; Kerekes & Douglas 1972). Since the stress exerted by a fibre on the fluid is sensitive to fibre orientation, it is important to understand the orientational motion of fibres in turbulent flows in order to accurately predict drag reduction.

In addition to these specific applications of fibre motion in turbulence, the subject has a fundamental interest. Most previous studies of particle motion in turbulence

have considered small spherical particles whose diameter is assumed to be much smaller than the Kolmogorov length scale. These 'point' particles have no orientation and respond only to the fluid velocity at one spatial position at any given time. A slender fibre represents the simplest system in which to investigate the orientation of non-spherical particles in a turbulent flow. It will also be seen that the equations of motion for a slender fibre give a relatively simple prescription for how this finite size particle responds to fluid flow over a finite range of spatial positions. In particular it will be seen that a fibre's translational velocity is a spatial average of fluid velocities along its length and its rotation depends on a first moment of the fluid velocity along its length.

Olson & Kerekes (1998) and Olson (2001) have considered the rotational and translational motion of fibres in an isotropic stochastic flow field which reproduces Kraichnan's (1970) energy spectrum. Olson & Kerekes derived analytical approximations for the rotational and translational dispersion coefficients. Olson tested these predictions using numerical simulations of fibre motion in a stochastic field produced by superimposing randomly selected Fourier modes. These studies reveal some of the qualitative trends that may be expected to influence fibre motion in turbulence. In particular, it was found that the translational and rotational dispersion coefficients decrease with increasing fibre length. We will re-examine some of the predictions of Olson & Kerekes and where possible improve on their approximate theories. An accurate determination of rotary dispersion requires simulations of fibre motion in a turbulent flow computed through direct numerical simulations such as those undertaken in the present study. It will be seen that fibres preferentially align with the rotational and extensional axes of the flow and this influences the fibres' rotational motions in ways that cannot be anticipated from a study based on an artificial stochastic flow field. The Kraichnan energy spectrum lacks an inertial subrange and does not mimic the spectrum in isotropic turbulence. By studying fibre motion in isotropic turbulent flows at several turbulence Reynolds numbers, we will try to identify the eddy length and time scales that contribute most to various measures of the fibres' rotational and translational motion.

In § 2 of this paper, we show how slender-body theory can be used to derive the equations of motion for a fibre in a turbulent flow field. The rotational dynamics constitute the unique feature of a study of orientable particles. However, we will also address (in § 3) the translational motion of the particles. Our interest in translational motion comes in part from a desire to compare and contrast translation and rotation. Particles are often used as tracers to visualize the motion of a turbulent fluid. In § 3.1, we determine how long a fibre would need to be in order that it no longer acts as a 'fluid tracer'. In particular, we consider the variance of the particle acceleration – an aspect of fibre motion that is influenced by the smallest eddies of the turbulent flow. In § 3.2, we consider the temporal auto-correlations of the particle acceleration and the particle velocity. Simple scaling analysis would suggest that the velocity is influenced by the largest eddies of the turbulent flow and acceleration by the smallest eddies. In keeping with this expectation, we will see that the correlation time for velocity scaled with the integral time scale is a function of the fibre length non-dimensionalized with the integral length scale. On the other hand, the correlation time for acceleration scaled with the Kolmogorov time scale is sensitive to the fibre length scaled with the Kolmogorov length scale. Section 3.3 gives results for the translational dispersion of fibres.

The rotary motion of the fibres is considered in § 4. We first examine the simplest measure of rotary motion – the variance of the particle rotation rate. Fibres rotate

due to fluid velocity gradients, which result primarily from Kolmogorov-scale eddies. Thus, we will see that the rotation rate variance scales with the square of the Kolmogorov shear rate. The rotation rate variance begins to decrease as the fibres become longer than the Kolmogorov length scale. If fibres are placed in the flow initially with random positions and orientations, the rotational motion is vigorous. However, the variance of the rotation rate slows down as the fibres align with the local axes of extension and rotation. On the basis of simple scaling arguments, one might expect the rotary dispersion coefficient, quantifying the temporal evolution of particle orientation, to depend on Kolmogorov length and time scales. However, the results of direct numerical simulations indicate no simple scaling for this important turbulence property, indicating that eddies of all scales contribute to rotary dispersion. In rotary Brownian motion of colloidal rods, there is a large separation between the time scale for the correlation of rotational velocity and the time over which the rods' orientations change appreciably. This separation of time scales is absent in turbulent rotary dispersion. As a result, turbulent dispersion cannot be characterized by a unique rotary diffusion coefficient and we examine several measures of rotary dispersion. It will be seen that the ratios of the various measures of rotary dispersion are $O(1)$ constants independent of the fibre length and the turbulence Reynolds number.

2. Simulation method

In § 2.1, we briefly review the standard method used to simulate stationary isotropic turbulence, define the relevant length and time scales, and summarize the conditions covered by our parametric study. Section 2.2 gives a derivation of the equations of motion for the fibres.

2.1. *Stationary homogeneous isotropic turbulent flows from DNS*

The incompressible Navier–Stokes equations are solved numerically using a pseudo-spectral method on a uniform three-dimensional mesh to generate a stationary homogeneous isotropic turbulent flow. In physical space, the solution domain is a cube of side 2π with N^3 grid points and periodic boundary conditions. A pseudo-spectral method is used to evaluate the nonlinear terms in the Navier–Stokes equations (Canuto *et al.* 1988). Since turbulent flows lose energy due to the viscous dissipation, an artificial forcing must be introduced in the Navier–Stokes equation to maintain statistically stationary turbulence (Eswaran & Pope 1988). Using 32^3 and 64^3 uniformly spaced grid systems, Reynolds numbers R_λ ($\equiv u'\lambda/\nu$) between 16.5 and 53.3 are obtained by varying the kinematic viscosity ν. Here u' is the r.m.s. value of the turbulent velocity and λ is the Talyor microscale.

In isotropic turbulent flows, the turbulent kinetic energy K and the dissipation rate ϵ can be determined from the three-dimensional energy spectrum, $E(k)$:

$$K \equiv \tfrac{3}{2}u'^2 = \int_0^\infty E(k)\,\mathrm{d}k, \tag{1}$$

$$\epsilon \equiv \langle\epsilon\rangle = 2\nu\int_0^\infty k^2 E(k)\,\mathrm{d}k, \tag{2}$$

where $k \equiv |\boldsymbol{k}|$ is the magnitude of the wave vector. The Eulerian integral length scale Λ associated with the two-point velocity correlation in the longitudinal direction

R_λ	16.5	30.7	39.9	53.3
N^3	32^3	32^3	32^3	64^3
ν	0.0524	0.0251	0.0165	0.0105
K	0.611	0.805	0.827	0.879
ϵ	0.174	0.182	0.175	0.174
λ	1.361	1.057	0.892	0.730
η	0.1704	0.0971	0.0719	0.0509
τ_η	0.556	0.376	0.314	0.248
Λ	1.768	1.604	1.483	1.405
τ_E	2.797	2.210	2.021	1.848
τ_L	2.073	1.784	1.552	1.444
$k_{max}\eta$	2.570	1.465	1.085	1.536
$\Delta t/\tau_\eta$	5.6×10^{-3}	8.4×10^{-3}	0.010	0.025

TABLE 1. The statistical quantities from the present simulations of stationary isotropic homogeneous turbulent flows.

(parallel to the velocity) and time scale τ_E are given by

$$\Lambda = \frac{\pi}{2u'^2} \int_0^\infty E(k) \frac{1}{k} \, \mathrm{d}k, \tag{3}$$

$$\tau_E = \frac{\Lambda}{u'}. \tag{4}$$

The Taylor microscale λ represents the area of a quadratic function, which fits the small separation region of the two-point velocity correlation in the longitudinal direction and decays from 1 to 0, and is given by

$$\lambda = \sqrt{3} u' (5\nu/\epsilon)^{1/2}. \tag{5}$$

The Kolmogorov scales in turbulence can be obtained by applying a dimensional analysis using dissipative properties ν and ϵ. The Kolmogorov length scale η representing the size of the smallest eddies is given as

$$\eta = (\nu^3/\epsilon)^{1/4}. \tag{6}$$

The Kolmogorov time scale τ_η, velocity u_η and shear rate Γ_η can also be obtained from the dissipative properties:

$$\tau_\eta = (\nu/\epsilon)^{1/2}, \tag{7}$$

$$u_\eta = (\nu\epsilon)^{1/4}, \tag{8}$$

$$\Gamma_\eta = (\epsilon/\nu)^{1/2}. \tag{9}$$

The conditions for our direct numerical simulations are summarized in table 1. The spatial resolution is characterized by $k_{max}\eta$, where $k_{max} = \frac{1}{3}\sqrt{2}N$ is the magnitude of the highest resolved wavenumber. Eswaran & Pope (1988) established that simulations with $k_{max}\eta$ larger than 1.5 corresponding to a grid spacing of about twice the Kolmogorov length scale give excellent resolution of the flow. Among our simulations, the case with the poorest spatial resolution is $R_\lambda = 39.9$ with $k_{max}\eta = 1.085$ corresponding to a grid spacing of about 2.7 times of η. A constant time step size Δt is used such that the worst temporal resolution is approximately $\frac{1}{40}$ of the Kolmogorov time scale. All the statistical quantities were obtained after the quantities acquired a statistical stationary state.

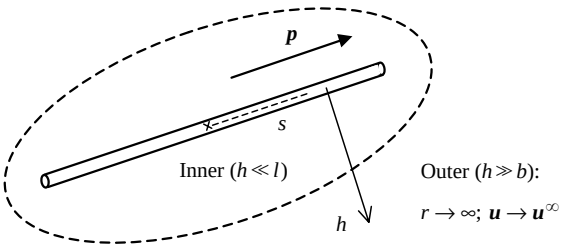

FIGURE 1. Schematic of the inner and outer regions of the flow around a fibre in slender-body theory.

We will investigate the translational and rotational motions of fibres with lengths L ($= 2l$) such that $L/2\pi = 7.96 \times 10^{-3}$, 1.59×10^{-2}, 7.96×10^{-2}, 0.159, 0.318, and 0.477. This corresponds to $L/\eta = 0.3$ to 18 and $L/\Lambda = 0.03$ to 1.7 for $R_\lambda = 16.5$ and to $L/\eta = 0.98$ to 59 and $L/\Lambda = 0.04$ to 2.1 for $R_\lambda = 53.3$.

2.2. *Equations of fibre motion*

We will simulate the motion of neutrally buoyant (force- and torque-free) fibres in isotropic turbulence. Because the volume of a fibre is a very small fraction of the sphere that circumscribes it, a fibre settles slowly. Thus, the neglect of sedimentation is not particularly restrictive. For example, polymer fibres (such as polyethylene oxide) with lengths $L = 1$ to 10 mm and diameters $d = 10$ to 100 μm have settling velocities of about 3×10^{-6} to 3×10^{-4} cm s^{-1} in water. Glass fibres with similar dimensions settle with velocities of $5 \times 10^{-5} \sim 5 \times 10^{-3}$ cm s^{-1} in water. Since the velocities associated with even a weak turbulent flow are on the order of 1 to 10 cm s^{-1}, one can usually neglect sedimentation velocities compared with turbulent velocities. We also consider the fibre concentration to be sufficiently small so that the fibres do not interact with one another hydrodynamically or through direct mechanical contacts.

We will use slender-body theory (Batchelor 1970) to derive equations of motion for fibres whose length L is much larger than their diameter d ($= 2b$). Slender-body theory is a matched asymptotic expansion with different asymptotic approximations in the inner and outer regions illustrated in figure 1. The inner region is at separations from the fibre, h, that are much smaller than the fibre half-length, $l = L/2$. The outer region is at separations much larger than the fibre radius, b. There is a matching region $b \ll h \ll l$ for which both the inner and outer solutions are valid. The local coordinate s is a position measured parallel to the fibre's axis that varies from $-l$ to l. It is assumed that viscous stresses dominate in the inner region and that the gradients in velocity and pressure along the fibre length are negligible compared with those perpendicular to the fibre. The finite thickness of the fibre does not influence the fluid velocity in the outer region. As a result, the fluid velocity in this region can be approximated as that produced by a line of forces distributed over the fibre axis.

Most previous applications of slender-body theory have considered viscous-dominated flows in both inner and outer regions. However, one can include inertial effects in the outer region of a slender-body theory provided that one has a method for solving the Navier–Stokes equations driven by the line of forces. Khayat & Cox (1989) used slender-body theory to determine the force and torque acting on a fibre translating through an otherwise quiescent fluid when viscous forces dominated in the inner region but inertia was important in the outer region. They solved the Oseen approximation to the Navier–Stokes equations to determine the leading behaviour of the fluid velocity for $\gamma = l/b \gg 1$. In the present application, we will also consider a

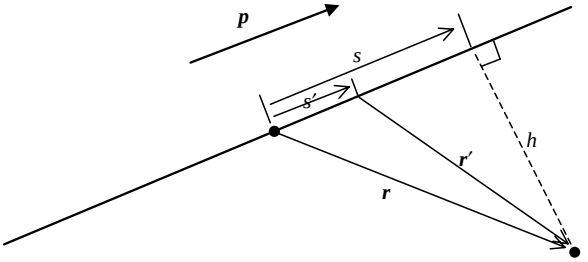

FIGURE 2. Schematic of the outer region in slender-body theory.

viscous-dominated inner region and an outer region that may be influenced by fluid inertia.

Viscous forces dominate in the inner region provided that a Reynolds number $Re_b(=u_c b/\nu)$ based on the fibre radius is much smaller than one. Here u_c is a characteristic velocity which for our application is equal to the characteristic velocity of an eddy of size L, i.e., $u_c \sim (\epsilon L)^{1/3}$. For fibres with lengths similar to the Kolmogorov length scale, $L = O(\eta)$, $u_c = u_\eta$, and $Re_b = O(1/\gamma) \ll 1$. If $L \gg \eta$, then $u_c = u_\eta (L/\eta)^{1/3}$ and $Re_b = O((L/\eta)^{1/3}/\gamma)$. Thus, there is still a viscous-dominated inner region provided that $\gamma \gg (L/\eta)^{1/3}$. For $Re_b \ll 1$, the fluid velocity in the inner region can be expressed as a quasi-two-dimensional solution of Stokes equations of motion, i.e.

$$u_i^{(in)} = U_i + \dot{p}_i s - \frac{1}{4\pi\mu} f_j(s)(\delta_{ij} + p_i p_j) \ln\left(\frac{h}{b}\right) + \frac{1}{4\pi\mu} f_j(s)\left(\frac{h_i h_j}{h^2} - \frac{\delta_{ij} - p_i p_j}{2}\right) + O\left(\frac{1}{h^2}\right), \quad (10)$$

where $\boldsymbol{U}$ denotes the translational velocity of the fibre centre of mass, $\dot{\boldsymbol{p}}$ the time rate of change of the fibre orientation vector, $\boldsymbol{p}$ the fibre orientation vector, $\boldsymbol{f}(s)$ the force per unit length along the fibre, and μ the dynamic viscosity of the fluid.

In the outer region ($h \gg b$), the flow field is three-dimensional and the inertial and viscous terms in the equations of motion are equally important. One cannot detect the finite thickness of the fibre, so that the stresses exerted on the fluid by the fibre can be treated as a line force. This outer solution can be obtained using a spectral code such as those typically used for simulating isotropic turbulent flows. The forcing in this spectral code would come both from the typical stochastic forcing used to produce the turbulence and from the lines of forces exerted by the fibres. In a future study we will investigate this two-way coupling problem. However, in the present study we will shortly show that the inertial modifications to the velocity disturbance caused by the fibres do not influence the fibre motion at leading order for slender fibres.

We express the outer approximation to the fluid velocity field (valid for $h \gg b$) as the sum of the fibre-induced fluid velocity disturbance that would occur in an inertialess fluid and an additional velocity u_i^E that arises from the turbulent flow field and the inertial corrections to the velocity produced by the fibre, i.e.

$$u_i^{(out)} = u_i^E(\boldsymbol{r}) + \frac{1}{8\pi\mu} \int_{-L/2}^{L/2} \mathrm{d}s' \left(\frac{\delta_{ij}}{r'} + \frac{r_i' r_j'}{r'^3}\right) f_j(s'), \quad (11)$$

where $r_i' = r_i - s' p_i$ (see figure 2). In our future two-way coupling calculation, $u_i^{(out)}$ will be obtained from the spectral code that includes forces due to the fibres as well as

a stochastic forcing and equation (11) will be used as a definition of u_i^E. By matching inner and outer solutions, we can obtain the integral equation for the fluid forcing exerted on the fibre.

Matching the inner and outer approximations to the fluid velocity and neglecting algebraically small terms in γ yields the following integral equation for the force distribution along the fibre length:

$$U_i + \dot{p}_i s = u_i^E(s) + \frac{1}{4\pi\mu}(\delta_{ij} + p_i p_j) f_j(s) \left(\ln 2\gamma + \ln \frac{\sqrt{1-s^2}}{b(s)} \right) + \frac{1}{8\pi\mu}(\delta_{ij} - 3p_i p_j) f_j(s) + \frac{1}{8\pi\mu}(\delta_{ij} + p_i p_j) \int_{-1}^{1} \mathrm{d}s' \frac{f_j(s') - f_j(s)}{|s' - s|}. \quad (12)$$

Here we non-dimensionalize s with the half-length l and the radius $b(s)$ with a characteristic radius, i.e. $b(s)$ in (12) is replaced simply with 1 in the case of a cylindrical fibre. If we solve this equation exactly, we will obtain the velocity, rotation rate, and force distribution with $O(1/\gamma^2)$ errors. However, to avoid a numerical solution of the integral equation, we can expand the solution in powers of $1/\ln 2\gamma$, thereby making logarithmic errors. The leading solution for the force is then

$$\frac{\ln 2\gamma}{4\pi\mu}(\delta_{ij} + p_i p_j) f_j(s) = U_i + \dot{p}_i s - u_i^E(s). \quad (13)$$

This solution has relative errors of $O(1/\ln 2\gamma)$. While this quantity is only moderately small for realistic values of the aspect ratio, it has been found in most applications that the leading approximation to slender-body theory yields reasonable predictions for the behaviour of fibres with aspect ratios larger than about 20.

We will consider fibres suspended in liquids. Since the volume of fluid set in motion by the translation and rotation of a fibre is a sphere of diameter L, the fluid inertia is much more important than the inertia of the fibre itself as long as the densities of the fibre and fluid are comparable. Thus, we will neglect the fibre's inertia. The force $\boldsymbol{F}$ and torque $\boldsymbol{G}$ exerted on the neutrally buoyant inertialess fibre will be zero:

$$F_i = \int_{-L/2}^{L/2} f_i(s)\,\mathrm{d}s = 0, \quad (14)$$

$$G_i = \int_{-L/2}^{L/2} \varepsilon_{ijk} f_j(s) p_k s\,\mathrm{d}s = 0. \quad (15)$$

Integrating (13) over the fibre and applying the constraint of no net force (14), the velocity of the centre of mass of the fibre is

$$U_i = \frac{1}{L} \int_{-L/2}^{L/2} u_i^E(s)\,\mathrm{d}s. \quad (16)$$

Multiplying (13) by $\varepsilon_{lim} p_m s$ and integrating over s, the rotation rate of the fibre is

$$\dot{p}_i = \frac{12}{L^3} \int_{-L/2}^{L/2} (\delta_{ij} - p_i p_j) u_j^E(s) s\,\mathrm{d}s. \quad (17)$$

Because the force exerted by the fibre is small, the contributions to $u_i^E(s)$ driven by the forces exerted by the fibre are smaller than the contributions due to the turbulent field by a factor of $1/\ln 2\gamma$. Thus, we will approximate $u_i^E(s)$ by the velocity field $u_i(s)$ evaluated by a spectral solution of the Navier–Stokes equation without the fibre forcing, i.e. a one-way coupling approximation. Olson & Kerekes (1998) and

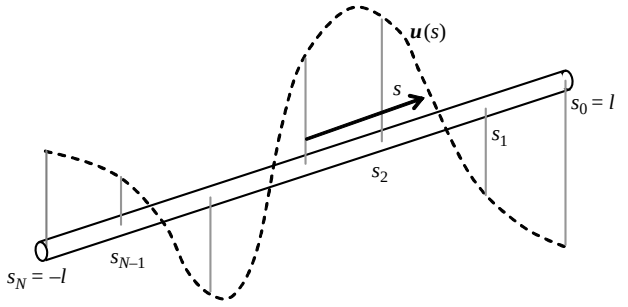

FIGURE 3. The polynomial approximation for the fluid velocity distribution along the fibre length.

Olson (2001) adopted (16) and (17) in their studies of fibre motion in a stochastic flow field. However, they presented these equations as analogous to the free-draining approximation in polymer science and did not provide the foregoing argument that these equations yield the leading-order behaviour for fibre rotation and translation in the limit $1/\ln 2\gamma \ll 1$.

The scheme outlined above could be made more accurate by including higher-order terms in the expansion of the integral equation (12) obtained from slender-body theory. The first effects of the fluid velocity disturbance produced by the fibres would arise at the next order, i.e. $O((1/\ln(2\gamma))^2)$ in the expansion. To be consistent then, one must include two-way coupling effects at the same time as increasing the accuracy of the slender-body theory. Such a calculation is planned for a forthcoming publication. The equations of fibre motion, (16) and (17), obtained above involve only the fibre length and not the fibre diameter. Thus, our results will be independent of the fibre aspect ratio. Of course the aspect ratio must be sufficiently large so that the leading approximation to slender-body theory is accurate (typically $\gamma > 20$). In addition the Reynolds number based on the fibre radius $Re_b = O((L/\eta)^{1/3}/\gamma)$ must be much smaller than one. For the longest fibres considered in our study this restriction amounts to $\gamma \gg 4$.

The most accurate means of determining the fibre velocity and rotation rate would be to express the fluid velocity in (16) and (17) in terms of its Fourier transform and perform the integrals over s to yield:

$$U_j = \sum_{\boldsymbol{k}} \hat{u}_j \exp(\mathrm{i}\,\boldsymbol{k}\cdot\boldsymbol{X}) \frac{\sin(\boldsymbol{k}\cdot\boldsymbol{p}l)}{\boldsymbol{k}\cdot\boldsymbol{p}l}, \tag{18}$$

$$\dot{p}_j = \sum_{\boldsymbol{k}} \frac{\mathrm{i}\,6}{L}(\delta_{jk} - p_j p_k)\hat{u}_j \exp(\mathrm{i}\,\boldsymbol{k}\cdot\boldsymbol{X}) \left\{ -\frac{\cos(\boldsymbol{k}\cdot\boldsymbol{p}l)}{\boldsymbol{k}\cdot\boldsymbol{p}l} + \frac{\sin(\boldsymbol{k}\cdot\boldsymbol{p}l)}{(\boldsymbol{k}\cdot\boldsymbol{p}l)^2} \right\}, \tag{19}$$

where $\hat{\boldsymbol{u}}$ is the Fourier transform of $\boldsymbol{u}$, $\boldsymbol{X}$ is the fibre centre of mass, and $\boldsymbol{k} = (k_1, k_2, k_3)$ is the wavenumber. However, the evaluation of the wavenumber sums for each fibre is very computationally intensive. Therefore, we adopted a more efficient algorithm, in which we approximate the velocity distribution along the fibre as an Mth-order polynomial (see figure 3):

$$u_i(s) = \sum_{m=0}^{M} a_{m,i} s^m. \tag{20}$$

The polynomial coefficients $a_{m,i}$ $(m = 0, 1, \ldots, M)$ are determined from the velocity data at $M+1$ fixed points which are distributed at equidistant intervals along the fibre

length. The velocity at each of these points is obtained by interpolating the velocity at 4^3 neighbouring grid points. A third-order method adopting tri-cubic shape functions is used to interpolate the data. Substituting (20) into (16) and (17), the velocity of the fibre centre and the rotation rate are expressed as

$$U_i = \frac{1}{L}\sum_{n=0}^{M} \frac{a_{m,i}}{m+1}\{l^{m+1} - (-l)^{m+1}\}, \tag{21}$$

$$\dot{p}_i = \frac{12}{L^3}(\delta_{ij} - p_i p_j)\sum_{n=0}^{M} \frac{a_{m,j}}{m+2}\{l^{m+2} - (-l)^{m+2}\}. \tag{22}$$

We tested this more efficient scheme by comparing the results from the inverse Fourier transform (18) and (19) with those from (21) and (22) for various orders of the polynomial. The velocity, position, orientation and rotation rate of the fibre computed from the scheme using $M \geqslant 5$ were identical with those from the Fourier representation. An eighth-order polynomial ($M = 8$) was used in the subsequent computational studies.

In the simulations, the statistics of fibre motion such as variances and correlations of fibre properties can be obtained by considering many fibres. Throughout the present work, the motions of 2000 fibres were computed simultaneously for each of 10 fluid flow realizations having different initial velocity fields to obtain accurate statistics for the various statistical quantities of fibre motions. Fibre motions in the turbulent flow fields were simulated for about $9\tau_E$ after the flow had achieved a stationary state. It was found that the fibre orientation equilibrated with the local flow after a period of $3\tau_E$. Unless otherwise noted, the statistics of fibre motion reported in this study correspond to the statistical steady state of the fibre motion achieved for $3\tau_E < t < 9\tau_E$.

3. Translational motion of the fibre

3.1. *Fibre acceleration variance*

Solid particles are often used as tracers to reveal the velocity of a fluid. It is therefore of fundamental interest to determine what types of particles will truly act like fluid tracers in a turbulent flow. Particles may deviate from the fluid motion due to their inertia or because the particle size becomes larger than the size of the smallest eddies. For neutrally buoyant spheres, both of these effects occur when the sphere diameter is comparable with the Kolmogorov length scale. For neutrally buoyant fibres, the fibre volume and mass are small enough that fibre inertia can be neglected when $L = O(\eta)$. However, fibres with $L \geqslant O(\eta)$ will respond to an average of the fluid velocity along the fibre length (see equation (16)) rather than the fluid velocity at the fibre centre. According to Kolmogorov scaling analysis, the acceleration of the fluid is controlled by the smallest eddies of size η. Thus, the variance of the acceleration of a particle is a simple but sensitive measure of how faithfully a finite size particle indicates the translational motion of a fluid particle.

It is natural to normalize the acceleration variance of the fibre's centre of mass, $\langle a^2 \rangle$ ($\equiv \frac{1}{3}\langle \boldsymbol{a} \cdot \boldsymbol{a} \rangle$), with the dissipation scales:

$$\langle a^2 \rangle^+ = \langle a^2 \rangle \frac{{\tau_\eta}^2}{{u_\eta}^2} = \langle a^2 \rangle \frac{\nu^{1/2}}{\langle \epsilon \rangle^{3/2}}, \tag{23}$$

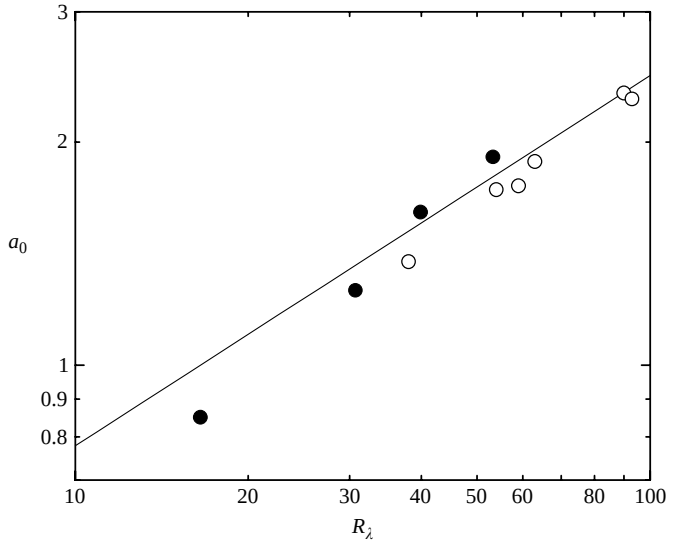

FIGURE 4. The acceleration variance a_0 of short fibres with $L < \eta$ is plotted as a function of R_λ together with the slope of $R_\lambda{}^{1/2}$ (solid line). The Kolmogorov-scaled variance a_0 is denoted by symbols: ●, $16.5 < R_\lambda < 53.3$ (present); ○, $38 < R_\lambda < 93$ (Yeung & Pope 1989).

where the angle bracket $\langle\cdot\rangle$ is the ensemble average and the superscript '+' indicates the non-dimensional acceleration variance. As the fibre length becomes less than η, $\langle a^2\rangle^+$ approaches the acceleration variance of a fluid particle, which we will denote as a_0. According to the Kolmogorov hypotheses (Kolmogorov 1941), at high Reynolds numbers, small-scale statistics non-dimensionalized by the Kolmogorov scales are universal. If the acceleration of the fluid particle is a dissipation-scale quantity, the constant a_0 must be independent of the Reynolds number. However, the acceleration variance of the fluid particle exhibits a strong Reynolds number dependence due to turbulent intermittency such that a_0 increases approximately as $R_\lambda{}^{1/2}$ at $38 \leqslant R_\lambda \leqslant 235$ (Yeung & Pope 1989 and Vedula & Yeung 1999). Figure 4 indicates that our results (solid circles) for a_0 follow the same scaling observed by Yeung & Pope (open circles). The recent experimental study of Voth *et al.* (2002) suggests that the Reynolds number dependence of a_0 is weaker or absent at very high Reynolds numbers ($R_\lambda \geqslant 500$).

When the fibre length exceeds the Kolmogorov length scale, the fibre acceleration becomes insensitive to the smallest scale velocity disturbances. This occurs because the fibre velocity is a spatial average of the fluid velocity over the fibre length as indicated by equation (16). The ratio of the variance of a fibre's acceleration to that of a fluid particle is plotted against the fibre length scaled by η in figure 5 for all of the Reynolds numbers simulated. As the fibre length increases, the fibre variance $\langle a^2\rangle^+$ starts to decrease from a_0. For $L/\eta < 15$, the acceleration can be fitted by a Gaussian function of fibre length:

$$\frac{\langle a^2\rangle^+}{a_0} \sim \exp\left[-\frac{1}{2W^2}\left(\frac{L}{\eta}\right)^2\right], \tag{24}$$

where W is the dimensionless width of the Gaussian. With the exception of the lowest Reynolds number simulated, a single Reynolds-number-independent Gaussian curve with $W = 20.6$ fits the data. This suggests that whereas the magnitude of the acceleration variance does not follow the expected Kolmogorov scaling, the

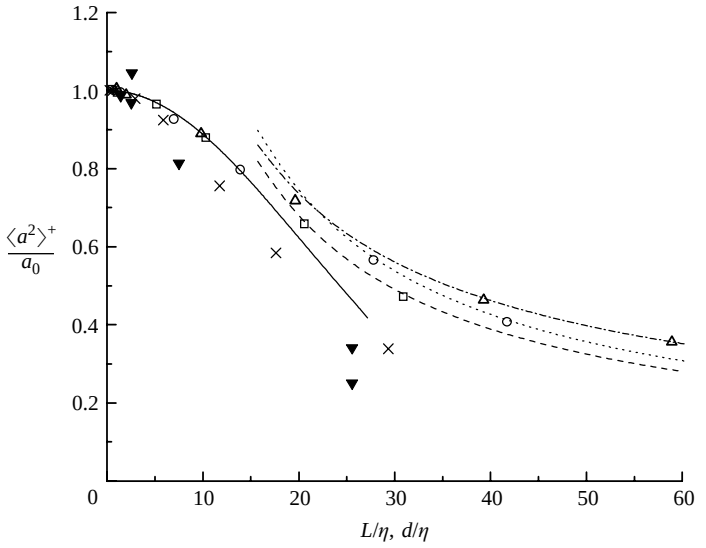

FIGURE 5. The fibre acceleration variance normalized by a_0 is plotted as a function of fibre length L. The open symbols denote the DNS results: $\times$, $R_\lambda = 16.5$; $\square$, 30.7; $\circ$, 39.9; $\triangle$, 53.3. The DNS data for $R_\lambda = 30.7 \sim 53.3$ are fitted to the Gaussian curve (solid line) for $L < 15\eta$. The solid symbols ($\blacktriangledown$) denote the experimental data for spherical particles with diameter d at $R_\lambda = 970$ (Voth *et al.* 2002).

Kolmogorov-scale eddies still do make a large contribution to the acceleration of a particle. The decay of the acceleration variance for longer fibres ($L > 20\eta$) is not universal. The fibre acceleration variance decays more slowly at higher R_λ as may be expected from the broader energy spectrum.

Figure 5 also gives Voth *et al.*'s experimental results for the acceleration variance of spherical particles with diameter d at a high Reynolds number ($R_\lambda = 970$). The density ratio of the particles and fluid was close to one. It can be seen that the experimental results for spheres show the same qualitative trend of decreasing particle acceleration variance with increasing particle size exhibited by our simulations for fibres. The acceleration variance for spheres decreases more rapidly with the ratio of the particle size to the Kolmogorov length scale than does the acceleration variance for fibres. This faster decrease may be attributed to two factors. First, if we assume that spheres, like fibres, respond to a spatial average of the fluid velocity over their volumes, the average of the fluid velocity for a sphere would be weighted more heavily toward velocities at its periphery. Thus, the sphere filters out high-wavenumber fluid velocities more strongly than does a fibre for the same maximum particle dimension. Second, the inertia of a spherical particle becomes important when $d = O(\eta)$ as indicated by the fact that the particle Stokes number takes an $O(1)$ value. The inertial spherical particle does not respond to the highest frequencies of the fluid velocity field. On the other hand, the small volume and mass of a neutrally buoyant fibre implies that its inertia is negligible even when $L = O(\eta)$.

3.2. *Correlation statistics for the fibre's translational motion*

We will now consider the two-time auto-correlations of the translational velocity and the acceleration of fibres as well as the associated correlation times. The auto-correlation function of fibre velocity is of interest because the integral of this function gives the translational dispersion coefficient which will be considered in the following

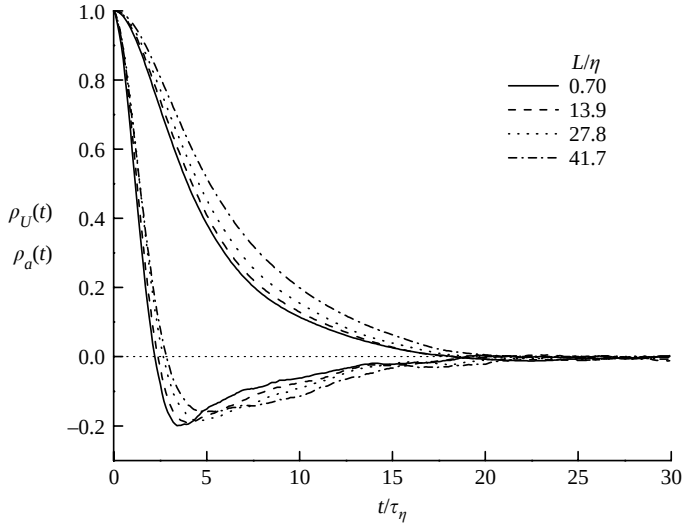

FIGURE 6. The Lagrangian auto-correlations of fibre velocity and acceleration for various fibre lengths at $R_\lambda = 39.9$. Upper curves denote $\rho_U(t)$ and lower curves denote $\rho_a(t)$.

subsection. Another motivation for considering the auto-correlations of velocity and acceleration is that they provide a useful comparison for the orientational statistics, i.e. the auto-correlations of the fibre's orientation and rotation rate.

The length scale of the eddies that give the largest contribution to the acceleration a, rotation rate $\dot{p}$, and velocity U of a fibre can be determined from dimensional analysis. In the inertial subrange, we assume these quantities depend only on the energy dissipation rate ϵ and the size l_e of the eddies yielding $a \sim (\epsilon^2/l_e)^{1/3}$, $\dot{p} \sim (\epsilon/l_e^2)^{1/3}$, and $U \sim (\epsilon l_e)^{1/3}$, where $\eta < l_e < \Lambda$. The characteristic acceleration and rotation rate grow with decreasing eddy size in the inertial subrange and are expected to be controlled by the Kolmogorov-scale eddies ($l_e \sim \eta$). Thus, we expect the correlation times for these quantities scaled with the Kolmogorov time scale to be functions of the fibre length scaled with the Kolmogorov length scale. The fibre velocity is the time integral of the acceleration and scaling analysis suggests that the fibre velocity is controlled by the large-scale eddies. We therefore expect that the correlation time for the fibre velocity scaled by the integral time is a function of the fibre length scaled by the integral length scale. The fibre orientation is the temporal integral of the fibre rotation rate. However, while velocity is a dimensional variable related to an unbounded translation, fibre orientation is a bounded, dimensionless variable. Thus, it is less clear how the correlation time for fibre orientation should scale and this subject will be investigated in § 4.2.

The Lagrangian correlation of a certain property A is defined as

$$\rho_A(t) = \frac{\langle A(t^*)A(t^*+t)\rangle}{\langle A(t^*)A(t^*)\rangle}. \tag{25}$$

The Lagrangian correlations of the velocity and acceleration of the fibre are calculated by computing the trajectories of many fibres in stationary homogeneous isotropic turbulent flows. Figure 6 illustrates the decaying behaviors of the correlations $\rho_U(t)$ and $\rho_a(t)$ at $R_\lambda = 39.9$. The translational motions of fibres with $L < \eta$ are identical to those of fluid particles and so $\rho_U(t)$ and $\rho_a(t)$ are equivalent to the corresponding correlation functions for fluid particles. The correlation functions for the acceleration

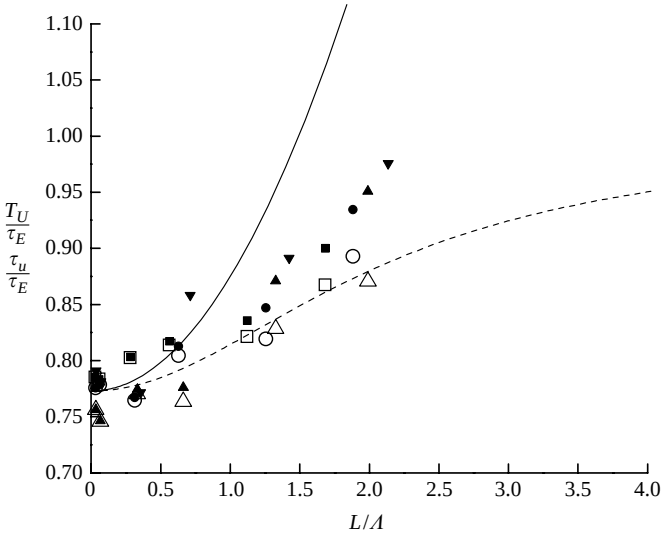

FIGURE 7. The integral time scales T_U and τ_u scaled by the Eulerian time scale τ_E are plotted as functions of the fibre length normalized by the Eulerian integral length scale Λ. The solid symbols denote the DNS data of T_U for different Reynolds numbers: ■, $R_\lambda = 16.5$; ●, 30.7; ▲, 39.9; ▼, 53.3. The open symbols denote the data for τ_u. The solid line is the fit (27) to the short-fibre behaviour of T_U. The dashed line is the fit (28) for τ_u.

and velocity of fibres with larger lengths decay more slowly than those of fluid particles. This may be attributed to the fact that longer fibres respond to a spatial average of the fluid velocity along their lengths. As a result, they are less sensitive to the smaller, faster-decaying eddies.

The integral time for the fibre's centre of mass velocity defined as

$$T_U = \int_0^\infty \rho_U(\tau)\,\mathrm{d}\tau \tag{26}$$

is a characteristic correlation time for fibre velocities. The correlation time scaled by the Eulerian integral time scale is plotted as a function of the fibre length scaled by the integral length scale in figure 7 for $R_\lambda = 16.5$ to 53.3. The results for fibre length less than Λ can be fitted approximately by a quadratic function

$$\frac{T_U}{\tau_E} = b_{U,0} + b_{U,2}\left(\frac{L}{\Lambda}\right)^2, \tag{27}$$

where the best fit is given by the coefficient values $b_{U,0} = 0.773$ and $b_{U,2} = 0.102$ independent of R_λ. While the statistical scatter leads to considerable uncertainty in the coefficients $b_{U,0}$ and $b_{U,2}$, there is no systematic variation of the data plotted in this way with R_λ whereas there is a systematic variation in T_U/τ_η for a given value of L/η with R_λ. This confirms our expectation that the translational motion of the fibre is controlled primarily by integral-scale eddies.

The increase in the fibre-velocity correlation time T_U with increasing fibre length L can be attributed to two factors: (*a*) changes in the way the fibre's centre of mass samples space; and (*b*) the fact that the fibre velocity is equal to a spatial average of fluid velocities. To isolate the former effect, we can consider the integral time τ_u for the fluid velocity at the fibre centre of mass. Short fibres with $L < \eta$ translate like fluid particles and have no variation of fluid velocity along their lengths, so that

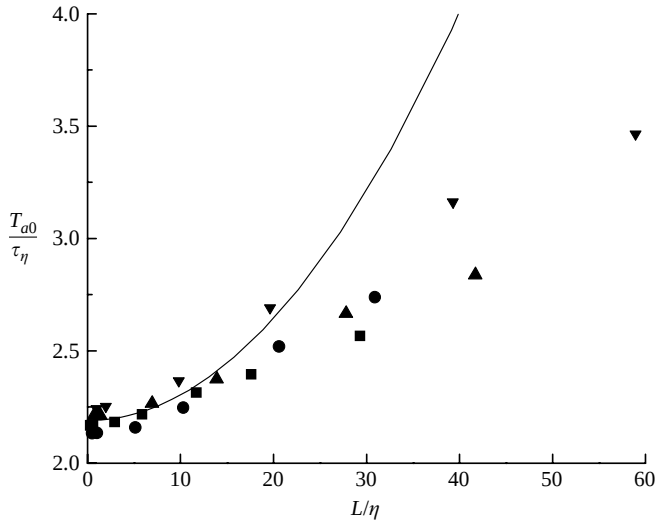

FIGURE 8. The zero-crossing time for $\rho_a(t)$ scaled by the Kolmogorov time scale τ_η is plotted as a function of fibre length normalized by the Kolmogorov length scale η. The symbols denote the DNS results for different Reynolds numbers: ■, $R_\lambda = 16.5$; ●, 30.7; ▲, 39.9; ▼, 53.3. The line denotes the fit for small fibres ($L/\eta < 15$) given by (29).

$T_U = \tau_u = \tau_L$ where τ_L is the Lagrangian correlation time for the fluid velocity. From the simulations, we find that $\tau_L = 0.773\tau_E$. As the fibre length increases, the fibre velocity becomes smaller. Eventually for $L \gg \Lambda$, the fibre velocity would approach zero and τ_u would approach the Eulerian correlation time for the fluid velocity τ_E. The DNS results for τ_u are plotted as the open symbols in figure 7. They can be fitted by the following functional form which approaches the appropriate limits as $L \to 0$ and $L \to \infty$:

$$\frac{\tau_u}{\tau_E} = 0.773 + \frac{b_1(L/\Lambda)^2}{b_1(L/\Lambda)^2/0.227 + b_2}. \tag{28}$$

Here $b_1 = 0.102$ and $b_2 = 2.01$ independent of R_λ. The increase in the data shown with the open symbols with L indicates the increase in the fibre-velocity correlation time that results from the slower rate at which the fibre samples spatial positions. The difference between the closed and open symbols indicates the increased correlation time resulting from spatial averaging effects. The similarity in the values of T_U and τ_u indicates that most of the variation of the correlation time for fibre velocity with fibre length can be explained by the changes in the way the fibre's centre of mass samples the fluid velocity field.

Next, we consider the temporal correlations of the fibre's acceleration. The integral of $\rho_a(t)$ cannot be used as a characteristic time for acceleration because the integral is zero. The acceleration is the time derivative of the velocity, so that $\rho_a(t)$ is negative for long time intervals where $\rho_U(t)$ has an upward curvature (Tennekes & Lumley 1972). Instead we take the time T_{a0} at which $\rho_a = 0$ (which will be referred to as the zero-crossing time) as a characteristic time for fibre acceleration.

The zero-crossing time for fibre acceleration scaled by τ_η is plotted as a function of fibre length scaled by η in figure 8. For the fibres with $L \lesssim 15\eta$, the zero-crossing

time T_{a0} shows a quadratic increase with the fibre length:

$$\frac{T_{a0}}{\tau_\eta} = c_{a,0} + c_{a,2}\left(\frac{L}{\eta}\right)^2. \tag{29}$$

The asymptotic value of T_{a0}/τ_η in the short-fibre limit, which is denoted by $c_{a,0}$ in (29), is 2.19 with no systematic Reynolds number dependence. The zero-crossing time for acceleration of short fibres, $T_{a0}/\tau_\eta = 2.19$ is in good agreement with the value of 2.2 for fluid particles reported by Yeung & Pope (1989). Yeung & Pope noted that the zero-crossing time is independent of R_λ while the minimum value of $\rho_a(t)$ increases with increasing R_λ. The coefficient $c_{a,2} = 1.125 \times 10^{-3}$ also is independent or R_λ. For $L \gtrsim 20\eta$, T_{a0} increases with L/η more slowly than the quadratic function in (29).

We have seen that the temporal correlations of fibre velocity and fibre acceleration are consistent with the expectation based on scaling analysis that the velocity and acceleration are controlled by integral- and Kolmogorov-scale eddies, respectively. The correlation times for both velocity and acceleration increase with increasing fibre length. These trends result in part from the fact that longer fibres are less sensitive to small-scale, rapidly fluctuating fluid motions. In addition, longer fibres have smaller velocities and sample spatial positions more slowly.

3.3. *Translational diffusivity*

We turn now to the translational dispersion of the fibre, which will be defined in terms of the time rate of change of the mean-square displacement of the particle's centre of mass, $\langle \Delta X^2 \rangle \equiv \langle \Delta \boldsymbol{X} \cdot \Delta \boldsymbol{X} \rangle$:

$$D_t = \frac{1}{6}\frac{\mathrm{d}\langle \Delta X^2 \rangle}{\mathrm{d}t}\bigg|_{t\to\infty}, \tag{30}$$

where $\Delta \boldsymbol{X} = \boldsymbol{X}(t) - \boldsymbol{X}(0)$. The translational dispersion of fibres is of interest in applications such as the spread long slender asbestos fibres, a form of indoor air pollutant. The dispersion coefficient was evaluated from the slope of $\langle \Delta X^2 \rangle$ versus time plots at large times when the mean-square displacement was found to grow linearly with time. The time required to reach a linear-slope region in $\langle \Delta X^2 \rangle$ is approximately equal to T_U. The DNS results for D_t normalized by the diffusivity of a fluid particle ($u'^2\tau_L$) indicated by the symbols are plotted as a function of fibre length, L/Λ in figure 9. For fibre lengths smaller than about 0.3Λ, the diffusivity D_t is the same as that of a fluid particle. As the fibre length increases, the dispersion decreases. The simulation results show no statistically significant dependence on R_λ when scaled with integral-scale quantities.

We now turn to an approximate theoretical estimate of the fibre diffusivity. From equation (30), the dispersion coefficient can be related to a time integral of the two-time auto-correlation of fibre velocity. Neglecting changes in the fibre orientation over the time interval τ and using the stationarity and homogeneity of the turbulent flow, we obtain

$$D_t = \frac{1}{3}\int_{-\infty}^{0} \langle U_i(0)U_i(\tau)\rangle \,\mathrm{d}\tau = u'^2\frac{4}{L^2}\int_{-\infty}^{0}\mathrm{d}\tau\int_0^L \mathrm{d}s(L-s)R(\boldsymbol{X}(\tau)+\boldsymbol{p}(\tau)s,\tau), \tag{31}$$

where $R \equiv \frac{1}{3}(R_{11}+R_{22}+R_{33})$ and $R_{\alpha\alpha}$ ($\alpha = 1, 2,$ or, 3) is the spatio-temporal velocity correlation measured along the trajectory of fibre's centre and its length, i.e.

$$R_{\alpha\alpha}(\boldsymbol{X}(\tau)+\boldsymbol{p}(\tau)s,\tau) = \frac{\langle u_\alpha(\boldsymbol{0},0)u_\alpha(\boldsymbol{X}(\tau)+\boldsymbol{p}(\tau)s,\tau)\rangle}{\langle u_\alpha(\boldsymbol{0},0)u_\alpha(\boldsymbol{0},0)\rangle}. \tag{32}$$

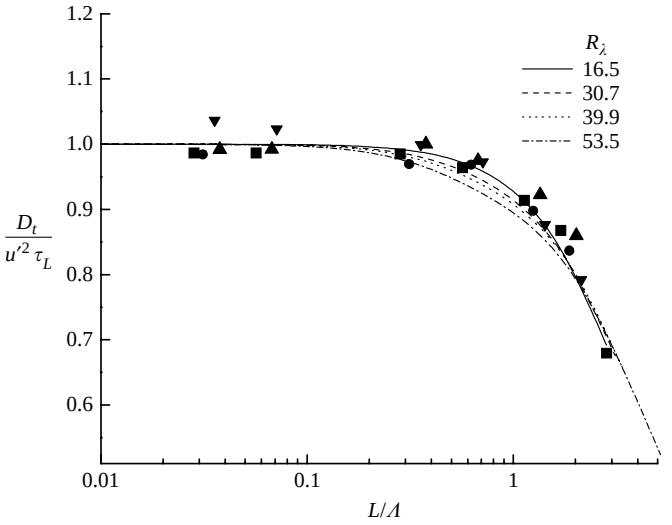

FIGURE 9. The long-time translational diffusivity D_t is plotted as a function of fibre length. The symbols denote the DNS results: ■, $R_\lambda = 16.5$; ●, 30.7; ▲, 39.9. ▼, 53.3. The lines denote the theoretical predictions based on (39).

We now approximate the velocity correlation function as the product of a term $R\big(\boldsymbol{X}(\tau), \tau\big)$ expressing the two-time correlation of velocity at the centre of mass of the fibre and a term $R(s\boldsymbol{p})$ giving the correlation of velocity between two points along the fibre length at a single time, i.e.

$$R(s\boldsymbol{p}(\tau) + \boldsymbol{X}(\tau), \tau) \simeq R(s)R(\boldsymbol{X}(\tau), \tau). \tag{33}$$

The time integral of $R(\boldsymbol{X}(\tau), \tau)$ simply gives the integral time τ_u for the fluid velocity at the fibre centre of mass. In the previous subsection we found that this quantity is described well by equation (28), which indicates that τ_u varies from the Lagrangian integral time at small L to the Eulerian integral time at large L. If we assume that the fibre orientation is independent of the direction of the fluid velocity, then the spatial velocity correlation function can be expressed as

$$R_{ij}(\boldsymbol{x}) = \frac{1}{u'^2}\int_{-\infty}^{\infty} \mathrm{d}\boldsymbol{k}\left(\delta_{ij} - \frac{k_i k_j}{k^2}\right)\frac{E(k)}{4\pi k^2}\,\mathrm{e}^{\mathrm{i}\boldsymbol{k}\cdot s\boldsymbol{p}}, \tag{34}$$

where $E(k)$ is the energy spectrum of the turbulent flow. The spatial velocity correlation can be decomposed into terms parallel and perpendicular to the fibre orientation:

$$R_{ij} = R_\parallel p_i p_j + R_\perp(\delta_{ij} - p_i p_j) \tag{35}$$

where

$$R_\parallel(s) = \frac{2}{u'^2}\int_0^\infty \mathrm{d}k\, E(k)\frac{1}{k^3 s^3}\{\sin(ks) - ks\cos(ks)\}, \tag{36}$$

$$R_\perp(s) = \frac{1}{u'^2}\int_0^\infty \mathrm{d}k\, E(k)\frac{1}{k^3 s^3}\{(k^2 s^2 - 1)\sin(ks) + ks\cos(ks)\}. \tag{37}$$

Since the spatial correlation $R(s)$ in (33) is an isotropic quantity, $R(s) = \frac{1}{3}R_{ii}(s)$.

R_λ	16.5	30.7	39.9	53.3
c_ζ	1.901	3.035	3.520	4.089
c_η	0.519	0.448	0.425	0.418

TABLE 2. The coefficients of c_ζ and c_η in (38) are determined by matching with the present DNS results for K and ϵ.

In order to calculate $R_\parallel$ and $R_\perp$, we use the energy spectrum $E(k)$ suggested by Pope (2000) which fits the available experimental data for isotropic turbulence:

$$E(k) = C\epsilon^{2/3}k^{-5/3}\left(\frac{k\zeta}{\sqrt{k^2\zeta^2 + c_\zeta}}\right)^{5/3+\alpha} \exp\left[-\beta\left\{\left(k^4\eta^4 + {c_\eta}^4\right)^{1/4} - c_\eta\right\}\right]. \tag{38}$$

This expression captures the appropriate shapes of the energy spectrum in the energy-containing and dissipation wavenumber ranges as well as the $k^{-5/3}$ dependence in the inertial subrange. Here $\zeta = K^{3/2}/\epsilon$ and the other constants are determined to recover the experimental data: $C = 1.4$, $\alpha = 2$, and $\beta = 5.2$. The remaining constants c_ζ and c_η can be determined by matching K and ϵ predicted by the model spectrum with the DNS results. Using the present DNS results for $R_\lambda = 16.5$, 30.7, 39.9 and 53.3, the constants c_ζ and c_η are determined for each R_λ and listed in table 2.

From (31) and (35)–(37), the long-time translational diffusivity, D_t, as a function of fibre length, can be written in terms of the energy spectrum $E(k)$:

$$D_t = \frac{4\tau_u(L)}{3L^2}\int_0^L \mathrm{d}s\,(L-s)\int_0^\infty \mathrm{d}k\,E(k)\frac{\sin(ks)}{ks}, \tag{39}$$

where $\tau_u(L)$ and $E(k)$ are given in (28) and (38), respectively. The theoretical predictions for D_t are plotted as the lines in figure 9 and compared with the DNS results. Because τ_u is dependent only on integral-scale quantities and the dominant contributions to the energy spectrum integral in (39) come from the energy-containing eddies, the theoretical results for $D_t/u'^2\tau_L$ are nearly independent of R_λ. As fibre length increases, the correlation time τ_u increases. However, the variance of the fibre velocity decreases with increasing L because it results from a spatial average over the fibre length. The decrease in the fibre velocity variance dominates the increase in the correlation time and the dispersion coefficient decreases with increasing L.

The translational diffusivity of the fibre can be expressed as a product of the variance of the velocity of the fibre $\langle U^2\rangle$ and the correlation time of the fibre velocity T_U. The approximation (39) for the diffusivity derived above involves two primary assumptions. First, the correlation time for the fibre velocity T_U is replaced by the correlation time for the fluid velocity at the fibre's centre of mass τ_u. This approximation is shown to be reasonably accurate in figure 7. Second, we neglect any correlation between the fibre orientation and the aspects of the fluid velocity that contribute to the fibre's velocity variance. This approximation may be expected to be accurate in most instances, since the fibre's velocity responds primarily to the large length scales of the turbulent flow while the fibre orientation is more sensitive to the small-scale eddies.

Olson & Kerekes (1998) derived an expression similar to (39) to predict the translational dispersion of fibres. Since they did not have an estimate for the correlation time for the fluid velocity at the centre of mass of the fibre τ_u, they replaced it with the Lagrangian integral time for a fluid particle. Olson (2001) found that Olson & Kerekes' formula did not give an accurate description of the fibre translational

dispersion he simulated in a stochastic flow field. We have shown that accounting for the dependence of τ_u on fibre length resolves this apparent discrepancy.

4. Rotational motion of the fibre

We now turn to the rotational dynamics of fibres in isotropic turbulent flows as indicated by the temporal evolution of a unit vector $\boldsymbol{p}(t)$ indicating the orientation of the fibre axis and the rotation rate (or time derivative of $\boldsymbol{p}$) which will be denoted as $\dot{\boldsymbol{p}}(t)$. In the next subsection we will discuss results for the simplest measure of the fibres' rotary motion, the variance of the fibre rotation rate $\langle \dot{p}^2 \rangle \equiv \langle \dot{\boldsymbol{p}} \cdot \dot{\boldsymbol{p}} \rangle$. In § 4.2, we will examine the R_λ-dependence of the correlation times for $\boldsymbol{p}$ and $\dot{\boldsymbol{p}}$ and compare them to the results for the correlation times for the acceleration and velocity of the fibre's centre of mass. This exercise will help us to understand which length scales of the turbulent flow contribute to the fibre's rotary dynamics. Finally, in § 4.3 we give results for several metrics of the turbulent rotary dispersion of fibres.

4.1. *Fibre rotation-rate variance*

Fibres are initially placed in a fully developed isotropic turbulent flow with randomly chosen positions and orientations. We will consider both the initial rotation rate variance ($t = 0$) and the asymptotic rotation rate variance that occurs after the fibre orientation has become correlated with the turbulent flow ($t \to \infty$).

4.1.1. *Short fibres*

We first analyse the initial rotation rate variance of fibres with lengths smaller than the Kolmogorov length scale $L < \eta$. The fluid velocity can be approximated as a linear function of position along the fibre length so that the fibre rotation rate is given by Jeffery's (1922) equation:

$$\dot{p}_i = \Gamma_{ij} p_j - p_i p_k S_{kl} p_l, \tag{40}$$

where $\Gamma_{ij} = S_{ij} + \Omega_{ij}$ is the velocity-gradient tensor and $S_{ij} = \frac{1}{2}(u_{i,j} + u_{j,i})$ and $\Omega_{ij} = \frac{1}{2}(u_{i,j} - u_{j,i})$ are the strain-rate and rotation-rate tensors, respectively. This expression for the rotation of a fibre with an asymptotically large aspect ratio is equivalent to the rotation rate of a fluid line. Thus, our results for short fibres will also indicate the rotational velocity variance of fluid lines. An expression for the variance of the rotation rate can be obtained by dotting the rotation rate from equation (40) with itself and taking the ensemble average to yield:

$$\langle \dot{p}^2 \rangle = \langle p_j p_l \Gamma_{ij} \Gamma_{il} \rangle - 2\langle p_i p_j p_l p_m \Gamma_{ij} S_{lm} \rangle + \langle p_i p_j p_l p_m S_{ij} S_{lm} \rangle. \tag{41}$$

At $t = 0$, the fibre orientation is uncorrelated with the directions of the local strain rate and rotation rate, so that each average in (41) can be decomposed into the product of an average of the orientation and an average of the velocity gradients, i.e.

$$\langle \dot{p}^2 \rangle(0) = \langle p_j p_l \rangle \langle \Gamma_{ij} \Gamma_{il} \rangle - 2\langle p_i p_j p_l p_m \rangle \langle \Gamma_{ij} S_{lm} \rangle + \langle p_i p_j p_l p_m \rangle \langle S_{ij} S_{lm} \rangle. \tag{42}$$

Since the fibre orientation distribution is isotropic, the moments of the orientation distribution can be related to the general isotropic second- and fourth-order tensors. We can then obtain a simple relationship between the initial rotational variance and the Kolmogorov shear rate:

$$\langle \dot{p}^2 \rangle(0) = \tfrac{1}{5}\langle S^2 \rangle + \tfrac{1}{3}\langle \Omega^2 \rangle = \tfrac{4}{15}\Gamma_\eta^{\,2}, \tag{43}$$

where we have used the fact that $\langle S^2 \rangle \equiv \langle S_{ij} S_{ij} \rangle = \langle \Omega^2 \rangle \equiv \langle \Omega_{ij} \Omega_{ij} \rangle = \frac{1}{2} \Gamma_\eta^{\,2}$ in an isotropic turbulent flow. Our simulation results indicate that $\langle \dot{p}^2 \rangle(0)/\Gamma_\eta^{\,2}$ is equal to 0.269 ± 0.014 independent of Reynolds number for $R_\lambda = 16.5$ to 53.3. These results for the initial rotation rate variance are in good agreement with the theoretical prediction (43) which yields the ratio 0.267.

As time progresses, the fibres rotate in the turbulent flow and a correlation develops between the orientation of the fibres and the local axes of the strain and rotation rates. It is then no longer possible to break the averages in (41) into independent averages of the velocity gradient and orientation statistics. We may expect that the rotation rate will slow as the fibres become aligned with the strain and/or vorticity field. Since the rotation rate of short fibres is still dependent on the local velocity gradient, we may expect that the rotation rate variance will still be proportional to the square of the Kolmogorov shear rate. In keeping with these expectations, the simulations indicate that the rotation rate variance achieved at long times after the introduction of the fibres into the flow is

$$\langle \dot{p}^2 \rangle(\infty)/\Gamma_\eta^{\,2} = 0.0963 \pm 0.0069, \tag{44}$$

independent of R_λ.

Since the rotation-rate variance of short fibres is controlled by the local velocity gradient following a particle that translates like a fluid particle, it provides an interesting test case for stochastic models that attempt to reproduce the fluid velocity gradient in a Lagrangian reference frame. Therefore, we have computed the long-time rotation-rate variance using (40) in conjunction with the stochastic models of Girimaji & Pope (1990) and Brunk, Koch & Lion (1998). Brunk *et al.* assumed that S_{ij} and Ω_{ij} were independent Gaussian variables satisfying isotropy and continuity conditions and reproducing the Lagrangian correlation times for the strain and rotation rates observed in DNS. This model has been shown to give accurate predictions for the rate of coagulation of pairs of particles due to turbulent shearing motions. Girimaji & Pope's model incorporates an approximate description of the correlation between the strain and rotation-rate tensors induced by the rotation and stretching of vortex lines, but does not yield the correct correlation time for the rotation rate. Simulations with Brunk *et al.*'s model yield a normalized long-time rotation-rate variance of 0.171 that is much larger than that obtained from DNS. This discrepancy is not surprising, because Brunk *et al.*'s model does not capture the correlation between the strain and vorticity axes. Thus, for example, a fibre's alignment with the straining field does not retard its rotation due to the vorticity. Girimaji & Pope's model yields a long-time variance of 0.0834 that is about 13 % smaller than the DNS result. A possible explanation for the slight discrepancy between the Girimaji & Pope model and the DNS can be found by considering the degree of alignment of the vorticity vector with the axes of strain. The strain axes can be characterized by the eigenvectors $\boldsymbol{q}_i$ and eigenvalues β_i where $\beta_1 > \beta_2 > \beta_3$ and typically $\beta_2 > 0$. It has been noted that the vorticity vector is preferentially aligned with $\boldsymbol{q}_2$ (Ashurst *et al.* 1987). This alignment would favour local flows in which the fibre would eventually approach a fixed orientation (i.e. strong flows) if the flow were not evolving with time. The mean angle between the vorticity and $\boldsymbol{q}_2$ in the DNS is 0.833 whereas the Girimaji & Pope model yields a mean angle of 0.615. If the vorticity and strain axes were uncorrelated, the mean angle would be 1. Thus, Girimaji & Pope's model overpredicts the alignment of vorticity with the second strain axis and may thereby overestimate the fraction of the fluid domain corresponding to strong, fibre aligning flows.

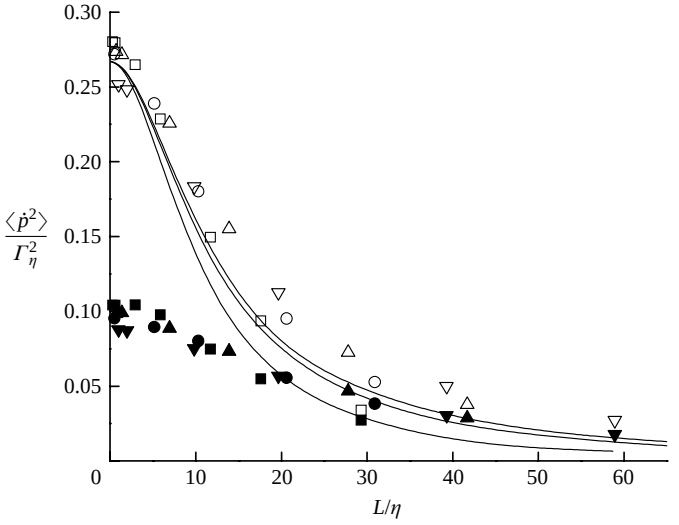

FIGURE 10. The initial and long-time variances of the fibre rotation rate are plotted as functions of fibre length, scaled by the Kolmogorov scales. The open and solid symbols denote the DNS results for the initial and long-time variances respectively: □, $R_\lambda = 16.5$; ○, 30.7; △, 39.9; ▽, 53.3. The lines are the theoretical predictions of initial rotation-rate variance. The lowest curve is for $R_\lambda = 16.5$ and the highest for $R_\lambda = 53.3$.

4.1.2. *Long fibres*

When the fibre length exceeds the Kolmorogov length scale, the fibre's rotation is influenced by the nonlinear dependence of the fluid velocity on spatial position. A long fibre does not rotate very much under the influence of a much smaller eddy and so the rotation-rate variance decreases with increasing fibre length. We can generalize the simple argument given above for the initial variance of short fibres to the case of longer fibres. From equation (17), the rotation-rate variance of a fibre can be expressed as

$$\langle \dot{p}_i \dot{p}_j \rangle = \frac{24}{L^3} \int_0^L \mathrm{d}s \left\{ 1 - 3\frac{s}{L} + 2\left(\frac{s}{L}\right)^3 \right\} \langle \xi_i(0,0,0) \xi_j(s, \boldsymbol{X}(t), t) \rangle, \tag{45}$$

where $\xi_i \equiv (\delta_{ik} - p_i p_k) u_k$. Initially the fibre orientation, $\boldsymbol{p}$, and the fluid velocity along the fibre, $\boldsymbol{u}$, are statistically independent. Using (33), the initial variance of the fibre rotation rate can be rewritten as

$$\langle \dot{p}_i \dot{p}_j \rangle(0) = u'^2 \frac{24}{L^3} \langle (\delta_{ik} - p_i p_k)(\delta_{jl} - p_j p_l) \rangle \int_0^L \mathrm{d}s \left\{ 1 - 3\frac{s}{L} + 2\left(\frac{s}{L}\right)^3 \right\} R_{kl}(s). \tag{46}$$

Employing the orthogonality between $\boldsymbol{p}$ and $\dot{\boldsymbol{p}}$, the initial variance of fibre rotation rate can be expressed as

$$\langle \dot{p}^2 \rangle(0) = u'^2 \frac{48}{L^3} \int_0^L \mathrm{d}s \left\{ 1 - 3\frac{s}{L} + 2\left(\frac{s}{L}\right)^3 \right\} R_\perp(s), \tag{47}$$

where $R_\perp(s)$ is the two-point spatial correlation for the velocity transverse to the fibre orientation given by (37).

The theoretical predictions for the initial fibre rotation-rate variance scaled by Γ_η^2 are plotted as a function of L/η as the solid lines in figure 10. The simulation results (open symbols) for the initial rotation-rate variance agree with the theory within

the statistical uncertainty of the simulations. Theory and experiment show a rapid decrease in the rotation-rate variance as L/η exceeds values of about 5. There is also a slight dependence of the rotation-rate variance on the Reynolds number for $L/\eta >$ about 5. The simulation results for the long-time rotation-rate variance of long fibres are plotted as the solid symbols in figure 10. The long-time rotation-rate variance also decreases with increasing L/η. However, the decrease is not as pronounced that of the initial rotation-rate variance and the two approach one another at very large fibre lengths.

The large differences between the initial and long-time rotational variances observed for short fibres can be attributed to a strong tendency of short fibres (acting like material lines) to align with the axes of the local velocity gradient field. The translational and rotational motions of long fibres are much less correlated with the fluid velocity field even at long times. Short fibres rotate primarily due to the Kolmogorov-scale eddies that produce the largest shear rates. Long fibres are less sensitive to the small-scale eddies due to the spatial averaging inherent in the fibre equation of motion (17). Thus, the rotational motion of long fibres is influenced by eddies with a range of lengths and the correlation of the fibre orientation with the axes of the flow on any of these length scales is imperfect. In addition, long fibres have a significant relative translational velocity with the fluid that decreases the time available for fibres to align with the flow. These factors explain the relatively small difference in the rotational velocity variance of long fibres initially placed in a random uncorrelated fashion into the flow and the rotational velocity variance of long fibres that have equilibrated with the flow.

4.2. *Correlation statistics of the rotational motion*

In this subsection we will consider the rotational dynamics of fibres in fully developed isotropic turbulence. We focus on the dynamics of fibres that have already interacted with the turbulence for an extended time period so that their alignment is correlated with the flow and they have reached a statistical steady state. A simple measure of the orientational changes incurred by the fibres is the two-time orientation correlation function $\rho_p(t)$. This correlation function is plotted as a function of time normalized by the Kolmogorov time scale for various fibre lengths and $R_\lambda = 39.9$ in figure 11. As the fibre length increases, the correlation in fibre orientation decays more slowly. This may be expected in view of the results from the previous subsection indicating that the rotation-rate variance decreases with increasing fibre length.

The two-time auto-correlation of the fibre's rotation rate, $\rho_{\dot{p}}(t)$, is also plotted in figure 11. Like the auto-correlation of fibre acceleration (see figure 6), $\rho_{\dot{p}}(t)$ is the correlation function for a variable that is the derivative of a stationary random process with a finite integral time scale. It therefore has a negative correlation at long times so that the integral of $\rho_{\dot{p}}(t)$ over time is zero (Tennekes & Lumley 1972). Nonetheless, it can be easily discerned from figure 11 that the correlations in the rotation rate are more long lived in longer fibres. The auto-correlation of $\dot{p}$ is plotted in figure 12 for short fibres ($L < \eta$) for the values of R_λ simulated in our study. The initial decay of the correlation of $\dot{p}$ including the zero-crossing time $T_{\dot{p}0}$ is approximately independent of R_λ. At longer times, higher R_λ flows yield a smaller negative minimum and a slower approach of the autocorrelation to zero.

The zero-crossing time for the fibre rotation-rate correlation normalized by the Kolmogorov time scale is plotted as a function of the fibre length divided by the Kolmogorov length scale in figure 13. This measure of the correlation time for rotation rate is independent of Reynolds number in this Kolmogorov scaling. For moderately

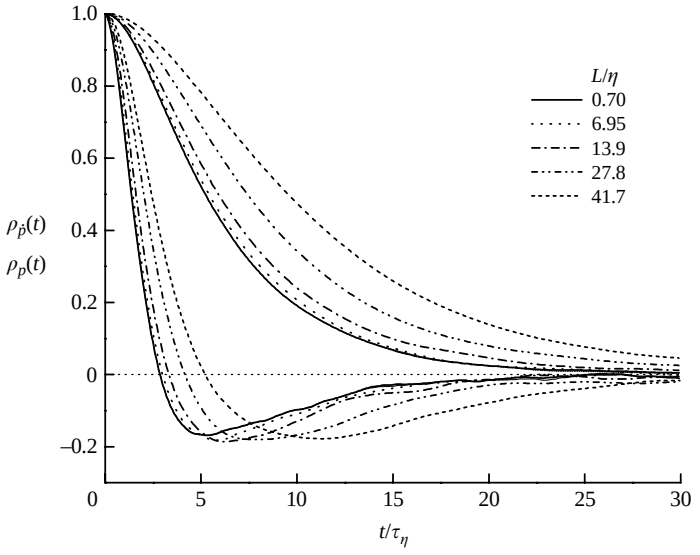

FIGURE 11. The Lagrangian auto-correlations of fibre orientation $\boldsymbol{p}(t)$ and rotation rate $\dot{\boldsymbol{p}}(t)$ for various fibre lengths ($R_\lambda = 39.9$). The upper curves denote $\rho_p(t)$ and the lower curves denote $\rho_{\dot{p}}(t)$.

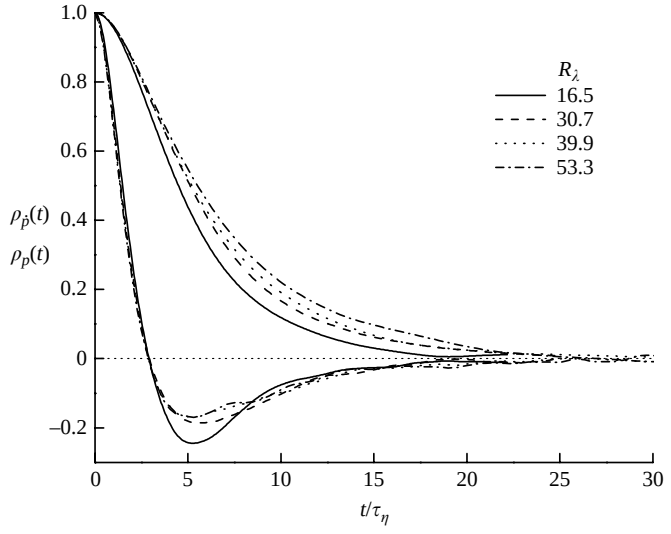

FIGURE 12. The Lagrangian auto-correlations of fibre orientation $\boldsymbol{p}(t)$ and rotation rate $\dot{\boldsymbol{p}}(t)$ for various Reynolds numbers. The upper curves denote $\rho_p(t)$ and the lower curves denote $\rho_{\dot{p}}(t)$ for short fibres ($L < \eta$).

small fibres ($L \lesssim 10\eta$), the zero-crossing time for rotation rate is fitted well by the quadratic asymptote

$$\frac{T_{\dot{p}0}}{\tau_\eta} = 3.01 + 0.0027\left(\frac{L}{\eta}\right)^2, \tag{48}$$

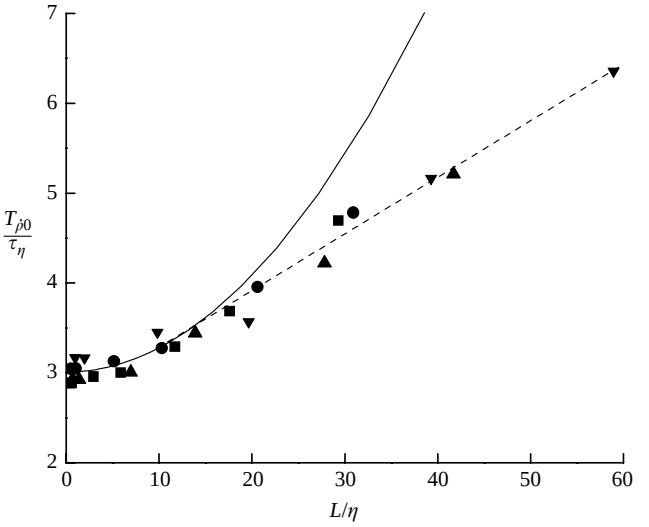

FIGURE 13. The zero-crossing time of $\rho_{\dot{p}}(t)$ is plotted as a function of fibre length, scaled by the Kolmogorov scales. The symbols denote the DNS results: ■, $R_\lambda = 16.5$; ●, 30.7; ▲, 39.9; ▼, 53.3. The solid line is the average quadratic asymptote (48) and the dashed line is the linear fit (49) for longer fibres ($L > 25\eta$).

while $T_{\dot{p}0}$ for longer fibres ($L \gtrsim 20\eta$) exhibits a linear dependence on fibre length:

$$\frac{T_{\dot{p}0}}{\tau_\eta} = 2.66 + 0.063\frac{L}{\eta}. \tag{49}$$

We will now examine in more detail the decay in the correlation of fibre orientation, $\rho_p(t)$. The auto-correlation of fibre orientation is plotted as a function of t/τ_η for short fibres in flows with various Reynolds numbers in figure 12. The correlation function $\rho_{\dot{p}}(t)$ is approximately independent of Reynolds number at times shorter than the zero-crossing time for rotation rate $T_{\dot{p}0} = 3\tau_\eta$. This behaviour is to be expected since the rotation-rate variance and $T_{\dot{p}0}$ both scale with Kolmogorov time scales. However, the longer time decay of the orientation correlation function exhibits a surprisingly strong dependence on R_λ over the range of Reynolds numbers explored in our simulations.

The integral time T_p for the fibre orientation is the simplest measure of the duration of a fibre's orientation auto-correlation in stationary isotropic turbulence. Previously, we have noted that dimensional analysis suggests that the correlation times T_{a0} and $T_{\dot{p}0}$ for fibre acceleration and rotation rate are controlled by the Kolmogorov scale and the correlation time T_U for the fibre velocity is controlled by the integral scale. Our DNS results for these quantities as a function of fibre length and R_λ confirmed these expectations. Because the fibre orientation is non-dimensional, one cannot directly discern which scales of turbulence influence it using the dimensional analysis that we applied to a, $\dot{p}$ and U at the beginning of § 3.2. However, we will see in the following subsection that the rotary dispersion coefficient D_{r0} is inversely proportional to T_p. Since D_{r0} has units of inverse time, one would expect the contributions to this quantity from eddies of size l_e in the inertial subrange to scale as $(\epsilon/l_e^2)^{1/3}$, similarly to $\dot{p}$. Thus, the rotary dispersion coefficient and T_p may be expected to be dominated by the smallest, Kolmogorov-scale eddies. This expectation is supported by the observations

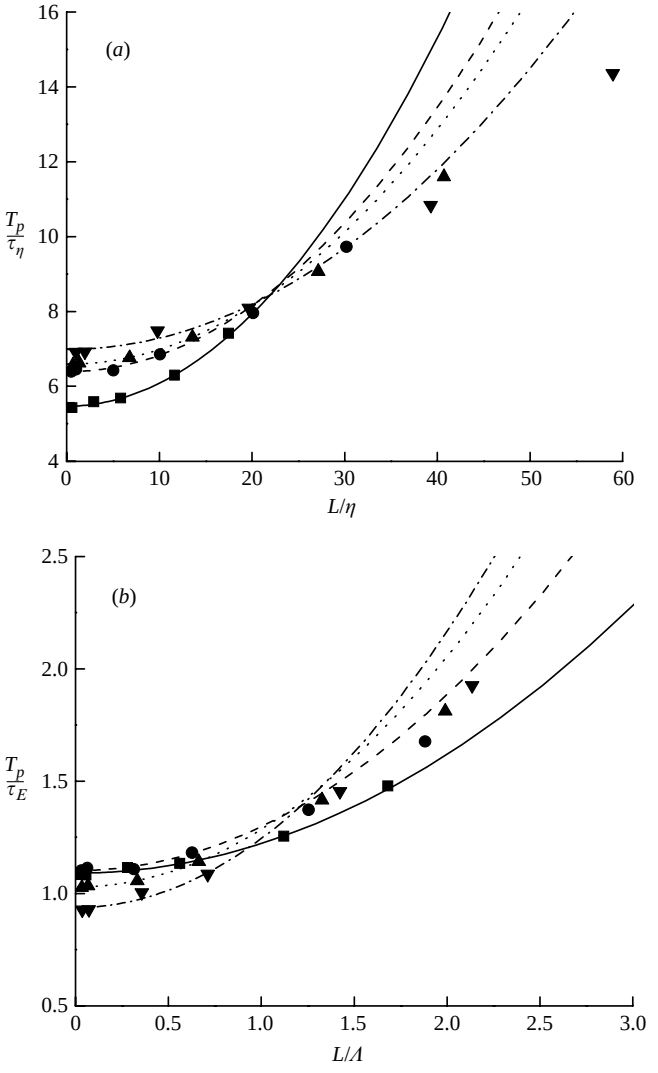

FIGURE 14. The integral time scale of the auto-correlation of fibre orientation, $\rho_p(t)$, is plotted as a function of fibre length, scaled by (*a*) Kolmogorov scales and (*b*) Eulerian integral scales. The symbols denote the DNS results: ■, $R_\lambda = 16.5$; ●, 30.7; ▲, 39.9; ▼, 53.3. The lines denote the quadratic asymptotes of the DNS data for each R_λ.

that the fibre's rotary dispersion results from the fibre rotational motions and that $\langle \dot{p}^2 \rangle$ and $T_{\dot{p}0}$ have been found to scale with Kolmogorov scales.

The fibre orientation integral time T_p is plotted as a function of fibre length L in figure 14. Figure 14(*a*) uses Kolmogorov time and length scales to non-dimensionalize the variables while figure 14(*b*) uses integral-scale quantities. It can be seen that neither scaling leads to results that are independent of Reynolds number. For short fibres, the integral time can be fitted by the quadratic asymptotes:

$$\frac{T_p}{\tau_\eta} = c_{p,0} + c_{p,2}\left(\frac{L}{\eta}\right)^2, \tag{50}$$

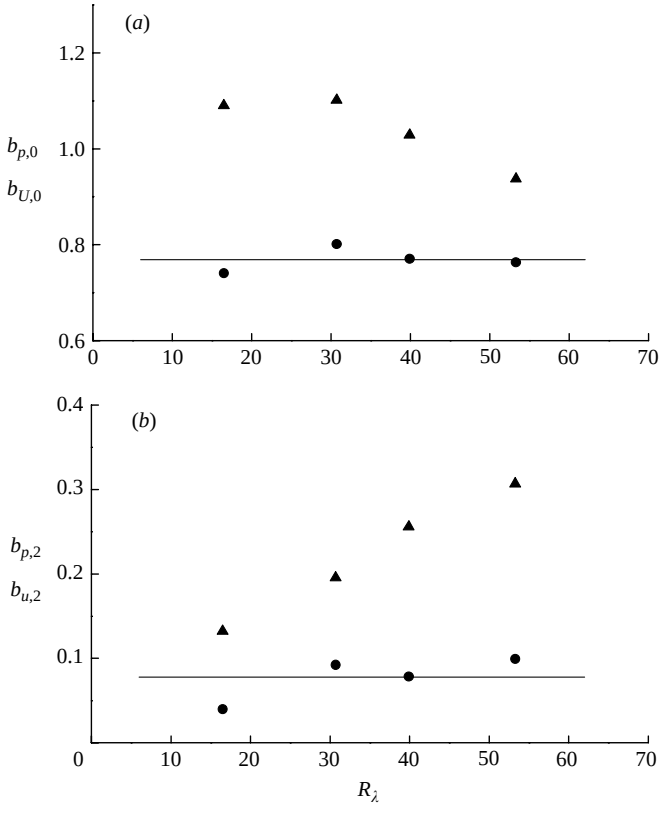

FIGURE 15. The coefficients of the quadratic asymptotes (27) and (51) are plotted as functions of R_λ: (*a*) for $b_{U,0}$ and $b_{p,0}$ and (*b*) for $b_{U,2}$ and $b_{p,2}$. The coefficients for the integral time scale T_U are denoted by ● and the coefficients for the integral time scale T_p by ▲. The lines indicate the average values $b_{U,0} = 0.773$ and $b_{U,2} = 0.102$.

and

$$\frac{T_p}{\tau_E} = b_{p,0} + b_{p,2}\left(\frac{L}{\Lambda}\right)^2. \tag{51}$$

However, $c_{p,0}$ increases and $c_{p,2}$ decreases with increasing R_λ, while $b_{p,0}$ decreases and $b_{p,2}$ increases with increasing R_λ. This suggests that, for the Reynolds numbers explored in our DNS study, the fibre's orientation correlation time is influenced by all the scales of turbulence and exhibits a scaling that is intermediate between Kolmogorov and integral scalings. Figure 15 compares the Reynolds number dependence of the coefficients $b_{p,0}$ and $b_{p,2}$ for the fibre orientation integral time with the corresponding coefficients for the fibre velocity. It can be seen that the coefficients for the fibre-velocity integral time is independent of R_λ when scaled with the large scales of turbulence whereas the coefficients for T_p exhibit a systematic dependence on R_λ.

Fibres rotate as a result of the velocity gradients in the turbulent flow. The largest velocity gradients occur in Kolmogorov-scale eddies. Thus, we might have expected T_p/τ_η to be a function of L/η independent of Reynolds number. It was found in § 4.1, however, that the rotation-rate variance decreased considerably as the fibre orientation became correlated with the axes of the local strain and vorticity fields. The

long-time rotation-rate variance of short fibres is about 36 % of the initial variance. Furthermore, as can be deduced from figure 10, the rotation rate occurring after the fibres have equilibrated with the flow is not as strongly dominated by small-scale eddies as one might have expected. Since the fibres rotate primarily due to eddies larger than their length, this value of $\langle \dot{p}^2 \rangle$ for fibres of length L may be taken as an indication of the ability of eddies larger than L to drive fibre rotation. It was found that $\langle \dot{p}^2 \rangle (t \to \infty)$ is a much weaker function of L/η than is $\langle \dot{p}^2 \rangle (t = 0)$. The small value of the long-time rotation-rate variance leads us to expect a large integral time for the auto-correlation of fibre orientation. Indeed we find in figure 14 that the value of T_p is similar in magnitude to the Eulerian integral time τ_E for the Reynolds numbers simulated here. If it is true that $T_p = \varphi \tau_\eta$ with φ of independent R_λ as $R_\lambda \to \infty$, then it appears that φ must be a large number and that this asymptotic behaviour would only be achieved at very high R_λ. It is not possible on the basis of the present DNS to distinguish between this possibility and a scenario in which T_p continues to be affected by intermediate scales of turbulence even as $R_\lambda \to \infty$.

4.3. *Rotary dispersion*

In this section we define and examine DNS results for several rotary dispersion coefficients characterizing the changes in fibre orientation induced by isotropic turbulence. We will define these coefficients by analogies with the rotary diffusivity of a Brownian fibre.

A Brownian fibre undergoes random rotational motions due to the forces exerted by the surrounding solvent molecules. The correlation time for the molecular forcing is much smaller than the viscous relaxation time of the particle (the time over which the rotation rate remains correlated). In turn, the viscous relaxation time is much smaller than the time $1/D_r$ over which $O(1)$ changes in the fibre orientation vector occur. These separations of time scales facilitate derivation of a simple governing equation for the probability distribution function $\Psi(\boldsymbol{p})$ for fibre orientation:

$$\frac{\partial \Psi}{\partial t} = D_r \nabla_p^2 \Psi, \tag{52}$$

where D_r is the rotary diffusivity and ∇_p $(= \boldsymbol{p} \times \partial/\partial \boldsymbol{p})$ is the gradient operator in fibre orientation space. The fibre orientation correlation function for a Brownian fibre can be obtained by solving (52) subject to the initial condition

$$\Psi(\boldsymbol{p}, 0) = \delta(\boldsymbol{p} - \boldsymbol{p}_0), \tag{53}$$

and then evaluating

$$\rho_p(t) = \langle \boldsymbol{p}(t) \cdot \boldsymbol{p}(0) \rangle = \frac{1}{4\pi} \int \mathrm{d}\boldsymbol{p} \int \mathrm{d}\boldsymbol{p}_0 \;\; \boldsymbol{p}(t) \cdot \boldsymbol{p}(0) \Psi(\boldsymbol{p}, t) \tag{54}$$

to yield

$$\rho_p(t) = \exp(-2 D_r t). \tag{55}$$

A non-Brownian fibre in isotropic turbulence undergoes stochastic rotary motions with no preferred direction for the orientational dynamics. In this way, turbulent rotary dispersion is similar to rotational Brownian motion. However, there is not a large separation of time scales between the correlation time for the rotation rate of a fibre in turbulence and the time required for the orientation to change significantly. In other words, Brownian fibres change their orientation due to many uncorrelated random rotations, whereas a fibre in turbulence has a significant change in orientation before the rotation-rate correlation function decays. Because of this distinction the

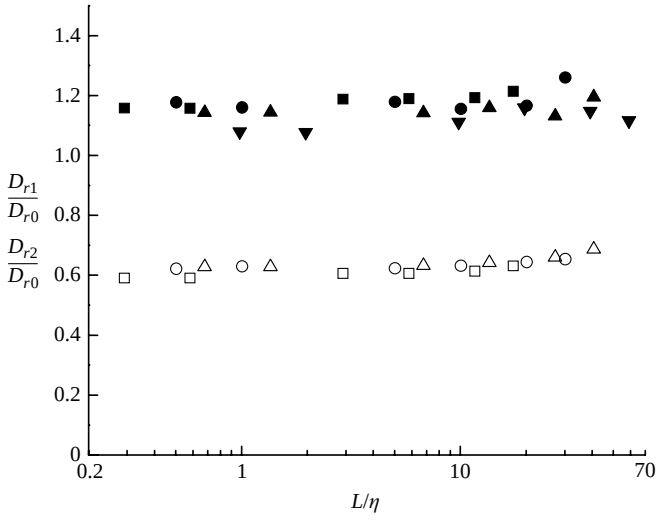

FIGURE 16. The ratios of rotary diffusivities D_{r1}/D_{r0} (solid symbols) and D_{r2}/D_{r0}(open symbols) are plotted as functions of fibre length. The Reynolds-number conditions are indicated by the shapes of the symbols: ■, $R_\lambda = 16.5$; ●, 30.7; ▲, 39.9; ▼, 53.3.

orientation correlation functions for fibres in turbulence (see figures 11 and 12) do not have an exponential dependence on time such as that obtained for Brownian fibres (55).

To define a rotary dispersion coefficient for fibres in turbulence, we can choose a value that would reproduce some particular feature of the fibre's orientation correlation function. For example, we may choose to define the rotary dispersion coefficient as the value of D_r that, when inserted into the governing equation for the orientation distribution of a Brownian fibre, would yield the same integral time for fibre orientation as that observed in the DNS. We will call this choice D_{r0} and it is given by

$$D_{r0} = \frac{1}{2T_p}. \tag{56}$$

The resulting values of D_{r0} can be readily determined by reading the values of T_p from figure 14.

An alternative definition of the dispersion coefficient (which we will call D_{r1}) focuses on the long-time decay of the orientation correlation function. At sufficiently long times, $\rho_p(t)$ obtained for fibres in DNS of isotropic turbulence was found to decay exponentially with time just as would occur for Brownian fibres. Thus, we can define a long-time dispersion coefficient as

$$D_{r1} = \lim_{t\to\infty} \frac{-1}{2t} \ln \rho_p(t). \tag{57}$$

Of course the statistical uncertainty in $\ln \rho_p(t)$ grows with increasing time. However, we were always able to obtain an accurate determination of the long-time plateau value of $-(1/2t)\ln \rho_p(t)$ before the statistical uncertainty became too large. The ratio of the long-time rotary dispersion coefficient D_{r1} to the dispersion coefficient D_{r0} based on the integral time for $\boldsymbol{p}$ is plotted as the solid symbols in figure 16. The ratio D_{r1}/D_{r0} is found to be about 1.2, independent of R_λ and L.

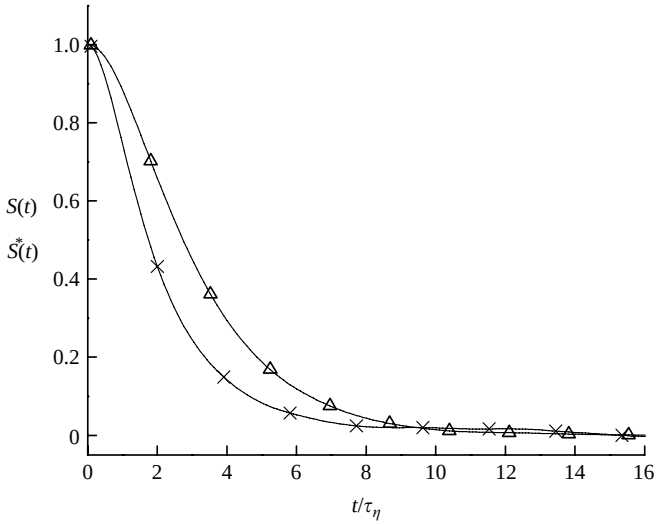

FIGURE 17. The order parameters S and S^* for $L/\eta = 0.69$ at $R_\lambda = 39.9$. Lines with symbols: $\triangle$, $S(t)$; $\times$, $S^*(t)$.

The fibre orientation correlation function $\rho_p(t)$ is a natural method of characterizing the dynamics of fibre orientation in the statistical steady state that occurs after fibres have interacted with the turbulence for a long time period. However, when describing the time evolution of an initially aligned suspension of fibres (e.g. $p_1 = p_2 = 0$, $p_3 = 1$), one commonly considers the order parameter defined as

$$S = \tfrac{3}{2}\langle p_3{}^2\rangle - \tfrac{1}{2}, \tag{58}$$

where the angle brackets indicate an average over the fibre orientation distribution function $\Psi(\boldsymbol{p})$. The order parameter is 1 if all the fibres are oriented in the 3-direction and 0 in an isotropic suspension. For a suspension of Brownian fibres that are initially aligned with the 3-axis, it can be shown that

$$S = \exp(-6D_r t). \tag{59}$$

We considered two types of simulation to explore the variation of the order parameter in a fibre suspension with time. In the first simulation, fibres were introduced into a stationary isotropic turbulent flow at random positions and with orientations parallel to the 3-axis in such a way that the fibre orientation was uncorrelated with the local turbulent shearing motion. The order parameter corresponding to this case is indicated by S^* and is plotted in figure 17. In the second type of simulation, motion of fibres was simulated in a turbulent flow for a long period of time so that the orientation of each fibre became correlated with the local flow. The 3-axis for a given fibre was then chosen to correspond to the fibre orientation at time $t = 0$. In this way, we simulate the behaviour that would occur in a fibre suspension where the fibres have a common alignment but are equilibrated with the flow. The order parameter corresponding to the latter simulation is indicated by S and is also plotted in figure 17. It can be seen that the order parameter S^* for fibres that are not pre-equilibrated with the flow decays faster than that of S for the fibres that have interacted with the flow before the initiation of the orientation experiment. This is to be expected in view of the decrease of the fibre's rotation-rate variance as the fibres interact with the turbulence (see § 4.1).

We can define a third rotary dispersion coefficient based on the dynamics of the order parameter in the pre-equilibrated fibre simulations. Denoting the time at which the order parameter decays to e^{-1} as T_{Se}, we define the order-parameter dispersion coefficient as

$$D_{r2} = \frac{1}{6T_{Se}}. \tag{60}$$

As shown in figure 16, the ratio of D_{r2} to D_{r0} (open symbols) is about 0.6 and is independent of Reynolds number and fibre length.

Over the range of Reynolds numbers explored in our study, the rotary dispersion coefficient D_{r0} based on the integral time scale for fibre orientation exhibits a significant Reynolds number dependence whether it is non-dimensionalized using τ_η or τ_E. The rotary dispersion coefficient also decreases with increasing fibre length. We have seen that there are a number of choices that can be made for the definition of the rotary dispersion coefficient. These different coefficients differ by $O(1)$ numerical factors. However, the three choices we have explored all exhibit the same dependence on R_λ and L.

5. Conclusion

We have presented results of direct numerical simulations for the translational and rotational motions of fibres in fully developed isotropic turbulence. Using slender-body theory, it was shown that the leading-order behaviours of the fibre's translational and rotational velocity obtained from an expansion in powers of $1/\ln(L/b)$ are expressed in terms of simple integrals involving the fluid velocity over the fibre length. Fibres whose lengths are much smaller than the Kolmogorov length scale translate like fluid particles and rotate like material lines. With increasing fibre length, the fibre's translational and rotational motions slow as the fibre becomes insensitive to the smaller-scale eddies. This results in a decrease in the fibre rotation-rate variance, rotary dispersion coefficient, translational diffusivity, etc. with increasing fibre length.

Simulations were performed for a range of Reynolds numbers in order to determine how various aspects of the fibre motion scaled with the length and time scales of the turbulence. The acceleration and rotary velocity of the fibre followed Kolmogorov scalings and the fibre velocity followed integral scalings as expected. One might expect the rotary dispersion coefficient to scale with the Kolmogorov time scale and depend on the ratio of the fibre length to the Kolmogorov length scale, because rotary dispersion results from the small-scale, local shearing motion of the fluid. However, the rotary dispersion coefficient (whether non-dimensionalized by τ_η or τ_E) was found to depend on the Reynolds number over the range of Reynolds numbers ($R_\lambda = 16.5$ to 55.6) explored in this study. As a fibre interacts with a turbulent flow, its orientation becomes correlated with the local strain and rotational axes, leading to a significant reduction in the rotational velocity variance. The fibre's rotation due to small-scale eddies is most strongly attenuated. The rotary dispersion is therefore smaller than one might have anticipated and is on the order of $1/\tau_E$.

It was found that a simple theory similar to that presented by Olson & Kerekes (1998) provided quantitative predictions for the translational diffusivity of the fibres. This theory neglects correlations of the fibre alignment with the direction of the fluid velocity and approximates the two-time, two-position fluid velocity correlation at different positions along the fibre length as the product of a one-time, two-position correlation and a two-time correlation for the fluid velocity at the fibre centre. To obtain quantitative predictions of the dispersion it was necessary to use a fit of the

simulation results for the integral time of the fluid velocity at the fibre centre. This quantity varies from τ_L to τ_E as the fibre length increases and the fibre's velocity variance decreases.

Olson & Kerekes presented a similar theory for the rotary dispersion of a fibre, assuming that the fibre's orientation was uncorrelated with the local axes of strain and rotation. Such a theory is not able to predict the rotary dispersion in a turbulent flow, however, because the correlations of the fibre axis with the strain and rotation-rate axes result in a significant slowing of the fibre's rotary motion. It was found that simulations based on a stochastic flow field (such as that of Brunk *et al.* 1998), which treat the fluids strain and rotation independently greatly over-estimate the rotary velocity of the fibres. On the other hand, Girimaji & Pope's stochastic model, which incorporates an approximate description of the correlations of the strain rate tensor and vorticity, resulting from vortex line stretching, gives a reasonable approximation to the rotation-rate velocity variance obtained in a turbulent flow. This observation suggests that Girimaji & Pope's model may be useful to investigators studying the behaviour of other complex fluids (such as polymer solutions) in turbulent flows.

This work was supported by NSF grant CTS-0332902 and by a postdoctoral fellowship to M. Shin granted by the Korea Science & Engineering Foundation (KOSEF).

REFERENCES

Ashurst, W. T., Kerstein, A. R., Kerr, R. M. & Gibson, C. H. 1987 Alignment of vorticity and scalar gradient with strain rate in simulated Navier–Stokes trubulence. *Phys. Fluids* **30**, 2343–2353.

Batchelor, G. K. 1970 Slender-body theory for particles of arbitrary cross-section in Stokes flow. *J. Fluid Mech.* **44**, 419–440.

Brunk, B. K., Koch, D. L. & Lion, L. W. 1998 Turbulent coagulation of colloidal particles. *J. Fluid Mech.* **364**, 81–113.

Canuto, C., Hussaini, M. Y., Quarteroni, A. & Zang, T. A. 1988 *Spectral Methods in Fluid Dynamics*. Springer.

Daily, J. W. & Bugliarello, G. 1961 The effects of fibres on velocity distribution, turbulence and flow resistance of dilute suspensions. *TAPPI.* **44**, 497–512.

Eswaran, V. & Pope, S. B. 1988 An examination of forcing in direct numerical simmulations of turbulence. *Computers Fluids* **16**, 257–278.

Girimaji, S. S. & Pope, S. B. 1990 A diffusion model for velocity gradients in homogeneous, isotropic turbulence. *Phys. Fluids* A **2**, 242–256.

Jeffery, G. 1922 The motion of ellipsoidal particles immersed in a viscous fluid. *Proc. R. Soc. Lond.* A **102**, 178–198.

Kerekes, R. J. E. & Douglas, W. J. M. 1972 Viscosity properties of suspensions at the limiting conditions for turbulent drag reduction. *Can. J. Chem. Engng* **50**, 228–231.

Khayat, R. E. & Cox, R. G. 1989 Inertia effects on the motion of long slender bodies. *J. Fluid Mech.* **209**, 435–462.

Kolmogorov, A. N. 1941 The local structure of turbulence in incompressible viscous fluid for very large Reynolds numbers. *Dokl. Akad. Nauk SSSR* **30**, 301–305.

Kraichnan, R. J. 1970 Diffusion by random fields. *Phys. Fluids* **13**, 22–31.

Mih, W. & Parker, J. 1967 Velocity profile measurements and phenomenalogical description of turbulent fibre suspension pipe flow. *TAPPI.* **50**, 237–246.

Olson, J. A. 2001 The motion of fibres in turbulent flow, stochastic simulation of isotropic homogeneous turbulence. *Intl J. Multiphase Flow* **27**, 2083–2103.

Olson, J. A. & Kerekes, R. J. 1998 The motion of fibres in turbulent flow. *J. Fluid Mech.* **377**, 47–64.

Pope, S. B. 2000 *Turbulent Flows*. Cambridge University Press.

Tennekes, H. & Lumley, J. L. 1972 *A First Course in Turbulence*. The MIT Press.

Vedular, P. & Yeung, P. K. 1999 Similarity scaling of acceleration and pressure statistics in numerical simulation of isotropic turbulence. *Phys. Fluids* **11**, 1208–1220.

Voth, G. A., La Potra, A., Crawford, A. M., Alexander, J. & Bodenschatz, E. 2002 Measurement of particle accelerations in fully developed turbulence. *J. Fluid Mech.* **469**, 121–160.

Yeung, P. K. & Pope, S. B. 1989 Lagrangian statistics from direct numerical simulations of isotropic turbulence. *J. Fluid Mech.* **207**, 531–586.